Spherulitic growth process in Ti-based metallic glass: Microstructure, phase identification, and growth mechanism

Laurabelle Gautier, Sophie Cazottes, Muriel Véron, Damien Fabrègue, Jérome Chevalier

Spherulitic growth process in Ti-based metallic glass: Microstructure, phase identification, and growth mechanism

Laurabelle Gautier, Sophie Cazottes, Muriel Véron, Damien Fabrègue, Jérôme Chevalier

PII: S1044-5803(22)00452-1

DOI: https://doi.org/10.1016/j.matchar.2022.112170

Reference: MTL 112170

To appear in: *Materials Characterization*

Received date: 20 April 2022

Revised date: 15 July 2022

Accepted date: 26 July 2022

Please cite this article as: L. Gautier, S. Cazottes, M. Véron, et al., Spherulitic growth process in Ti-based metallic glass: Microstructure, phase identification, and growth mechanism, *Materials Characterization* (2022), https://doi.org/10.1016/j.matchar.2022.112170

Spherulitic growth process in Ti-based metallic glass: microstructure, phase identification, and growth mechanism

Laurabelle Gautier[1], Sophie Cazottes[1*], Muriel Véron[2], Damien Fabrègue[1], Jérôme Chevalier[1]

[1] INSA-Lyon, MATEIS Laboratory, Materials Department, Institut National des Sciences Appliquees de Lyon, University of Lyon, UMR CNRS 5510, 20 Avenue Albert Einstein, Villeurbanne CEDEX 69621, France
[2] SIMAP Laboratory, CNRS-Grenoble INP, BP 46 101 rue de la Physique, 38402 Saint Martin d'Hères, France
*Corresponding author, sophie.cazottes@insa-lyon.fr

Abstract:

$Ti_{40}Cu_{36}Zr_{10}Pd_{14}$ metallic glass is often considered a promising candidate for biomedical applications, in particular for the manufacturing of small size dental implants. Nevertheless, its processing and limited glass-forming ability leads to the appearance of crystalline spheres called "spherulites". These spherulites play a major role in the deformation behaviour of this alloy. It is therefore a critical issue for its future industrial use to identify their nature and better understand their growth process to enable control of their size distribution and localisation. This article presents a detailed description of the microstructure of these crystalline defects, from the sub millimetre to nanometric scales, using transmission electron microscopy (TEM), energy-dispersive X-ray spectroscopy (EDS)/electron backscatter diffraction (EBSD) coupled with scanning electron microscopy and X-ray diffraction characterisation. Several phases are identified thanks to the combination of EDS/EBSD and TEM information, in particular a CuTi B2 phase analogous to the ZrCu B2 phase usually present in other composite metallic glasses. The presence of other phases such as Ti_2Cu_3 and $CuTi_3$ phases is also detected. The spherulites are studied at different times during their growth process, and a growth scenario is proposed based on the characterisation observations. However, the nucleation step of the spherulites remains unclear despite the in-depth investigation. Thus, different hypotheses are discussed.

Keywords:

TiCuPdZr, Bulk metallic glasses, Crystalline defect, microstructure, spherulite, eutectoid

Introduction:

Metallic glasses are widely recognised as having a far superior elastic limit compared with their crystalline counterparts, making them particularly attractive for biomedical, luxury, high-performance sports, and wear-part applications [1]. Most bulk metallic glass (BMG) grades offer good corrosion resistance [2] and the ability to deform without crystallising near their glass-transition temperature (T_g) [3]. The alloy $Ti_{40}Zr_{10}Cu_{36}Pd_{14}$ exhibits good biocompatibility together with a very high elastic limit (approximately 2 GPa, mostly measured in compression) and a low Young's modulus (approximately 100 GPa) [4]. It is therefore an interesting candidate for the manufacture of dental implants of reduced size, *i.e.,* with less impact on the implantation site. This composition was discovered by Inoue and collaborators [5] to offer an alternative to the current crystalline alloys, which contain non-biocompatible atomic species such as aluminium, vanadium, nickel, cobalt, and chrome [6].

Although many BMG grades have been shown to be fully amorphous, even for specimens presenting quite large diameters (several millimetres), certain other grades are only partially amorphous, such as Cu–Zr- and Cu–Ti-based BMGs [7]. In the alloy $Ti_{40}Zr_{10}Cu_{36}Pd_{14}$, large spherical crystalline defects (later called spherulites), which can be several hundreds of micrometres in diameter, are unfortunately often present (even in quite small samples) and are randomly dispersed in the as-cast rods [8]. They cannot be observed using standard X-ray diffraction (XRD) techniques or after compression testing; nevertheless, they clearly affect the tensile strength and fatigue properties [8]. Preliminary observations have revealed that spherulites are most likely composed of a cubic phase (CFC structure, 3.14-Å lattice parameter). Inside the spherulites, a fine submicrometric microstructure has been observed but not yet detailed, revealing that several phases may coexist. To date, the exact nature of the spherulites and their formation mechanism remains undescribed. According to Sypien *et al.* [9], the differential scanning calorimetry (DSC) curves for this alloy (initial amorphous state) revealed several crystallisation peaks, indicating the presence of different phases. The phases identified in [10] were all from the CuTi binary phase diagram, under the assumption that Zr atoms substitute at Ti sites and Pd atoms substitute at Cu sites. This strong assumption allowed Sypien *et al.* to reveal the presence of the $(Ti,Zr)_3(Cu,Pd)$, $Ti_2(Cu,Pd,*)$, and $(Ti,Zr)_2(Cu,Pd)$ phases from scanning electron microscopy (SEM)–energy-dispersive X-ray spectroscopy (EDS) measurements. The reason for the proposed phases is the large solubility of Pd and Cu [11] and Ti and Zr [12]. However, no crystallographic evidence for the presence of those phases has been provided.

Premature failure can be observed in the $Ti_{40}Zr_{10}Cu_{36}Pd_{14}$ alloy, with severe consequences for the biomedical applications targeted [4]. As the spherulites deform plastically [13], if their size is controlled and limited, they could allow global plasticity of the specimen before failure. This would require the optimisation of the spherulite size and volume fraction during the specimen elaboration.

The aim of this study was to provide a multi-scale microstructural characterisation of the spherulite from the sub millimetre to nanometric scale. The microstructure of the spherulites formed in a $Ti_{40}Cu_{36}Zr_{10}Pd_{14}$ BMG alloy was observed using optical and electron microscopy. Two different types of crystalline defects were observed: large-scale spherulites (almost millimetric, already well developed) and spherulite precursor dendrites (~50 µm in length). Focused ion beam (FIB) thin foils, extracted at the centre and surface of the spherulites, were used to identify the phases present. The information gathered was used to propose and discuss a scenario for the growth of spherulites as well as hypotheses for their nucleation.

1. Materials and methods

Sample preparation and casting

Ingots with a targeted composition of $Ti_{40}Zr_{10}Cu_{36}Pd_{14}$ (at.%) were prepared by arc melting from previously washed pure elements (purity above 99.9%). Rods with 3-mm diameter were prepared using a suction copper mould-casting apparatus (Arc melter AM 200, Edmund Bühler GmbH, Bodelshausen, Germany), with a primary vacuum below 5 x 10^{-2} mbar and a secondary vacuum below 5 x 10^{-5} mbar. Before switching on the electric arc, the chamber was filled with 0.7 bar of high-purity argon atmosphere. The current intensity was 200 A, and raw materials were melted 4 times for 30 s each time to obtain the master alloy. The master alloy was melted again two times before casting.

Optical microscopy

Optical microscopy (OM) observations were conducted after different polishing steps on a Buehler semi-automatic polishing machine Ecomet 250 (Esslingen, Germany), first with SiC papers successively with grains of #600, #800, #1200, and #2500 grit. The final mechano-chemical polishing step was performed on a Buehler ChemoMet synthetic polishing pad with a solution made of 75% colloidal silica suspension (OP-S) and 25% H_2O_2. Observations were performed using an Hirox RH-2000 digital microscope (River Edge, NJ, USA).

X-ray diffraction

After the BMG rods were fabricated, XRD was performed on a Bruker AXS D8 (Billerica, Massachusetts, USA) device equipped with a copper tube on a zone of the sample where the density of spherulite was high and identified thanks to OM. The X-ray tube was set at a voltage of 4 KeV and a current of 40 mA with Cu K_α radiation of 1.54 Å wavelength. The detector used was a Lynxeye, which was used over a 2θ range from 10° to 90° with an increment of 0.0167°, with a slit of 0.4 mm and a scan speed of 1 s/step. The post-acquisition processing of the diffractograms was conducted on Eva software (Bruker). The Rietveld method was performed on Topas software (Bruker).

Scanning electron microscopy

The polished surfaces were examined using SEM (Zeiss Supra 55, Oberkochen, Germany), in backscattered electron imaging (BSE) mode using an acceleration voltage ranging from 10 to 30 keV, after polishing using silica suspension and 25% H_2O_2 (as described in the OM section).

Energy-dispersive X-ray spectroscopy

To ensure that the composition of each sample was consistent with the desired one and that no vaporisation of elements had occurred during the processing of the master alloy, the compositions of all the cast rods were controlled using EDS using a 50 mm² silicon drift detector (Oxford Instruments, High Wycombe, UK) in the scanning electron microscopy at an acceleration voltage of 20 keV. Moreover, EDS was used to quantify the chemical composition of the different phases present.

Electron backscattered diffraction

Electron backscattered diffraction (EBSD) analyses were performed using an Oxford Instruments EBSD Symmetry camera (Abingdon-on-Thames, UK) with an accelerating voltage of 10 or 20 keV, depending on the step size required. The EBSD data were post-processed using ATEX [14].

Phase identification for a non-equilibrium state with four different components is a difficult task. To identify possible candidates for the different phases observed, a strong hypothesis was made, which is that the minor elements (Zr and Pd) would substitute for the major elements (Cu and Ti) [15]. This rather strong assumption was necessary to identify possible candidates from the Cu–Ti system among all possible structures in the literature. It is worth noting that this assumption is quite classical and can be found in the literature on alloys with a composition close to the one studied here [15–17]

Phase identification was performed using the phases presented in Table 1.

Table 1: Candidate phases used during this study.

Phase name	Space group	a(Å)	c (Å)	Reference
Cu_3Ti_2	I4 m m m	3.14 Å	13.962 Å	[18]
tetragonal CuTi	P 4/m m m	3.14 Å	2.856 Å	[19]
$CuTi_3$	P 4/m m m	4.158 Å	3.594 Å	[19]
CuTi-B2	Pm-3m	3.14 Å	3.14 Å	[20] from CuZr adjusted

TEM

The FIB thin foils were prepared on a FEI Strata DB 235 at IEMN laboratory (Lille, France) using a Ga FIB source. TEM observations were performed on a JEOL 2010F TEM operating at 200 kV, equipped with a 60 mm² Oxford Instrument EDS detector.

MET ASTAR

At the TEM scale, orientation maps were acquired with the ASTAR system from NanoMEGAS SPRL (Brussels). With this TEM attachment, the electron beam is scanned over the area of interest and the successive diffraction patterns are recorded with an optical camera and memorised. Phase and/or orientation maps are reconstructed by indexing the patterns with a dedicated template matching algorithm [21]. ASTAR acquisitions were performed on a field-emission transmission electron microscope at 200 kV (JEOL 2100F).

2. Results

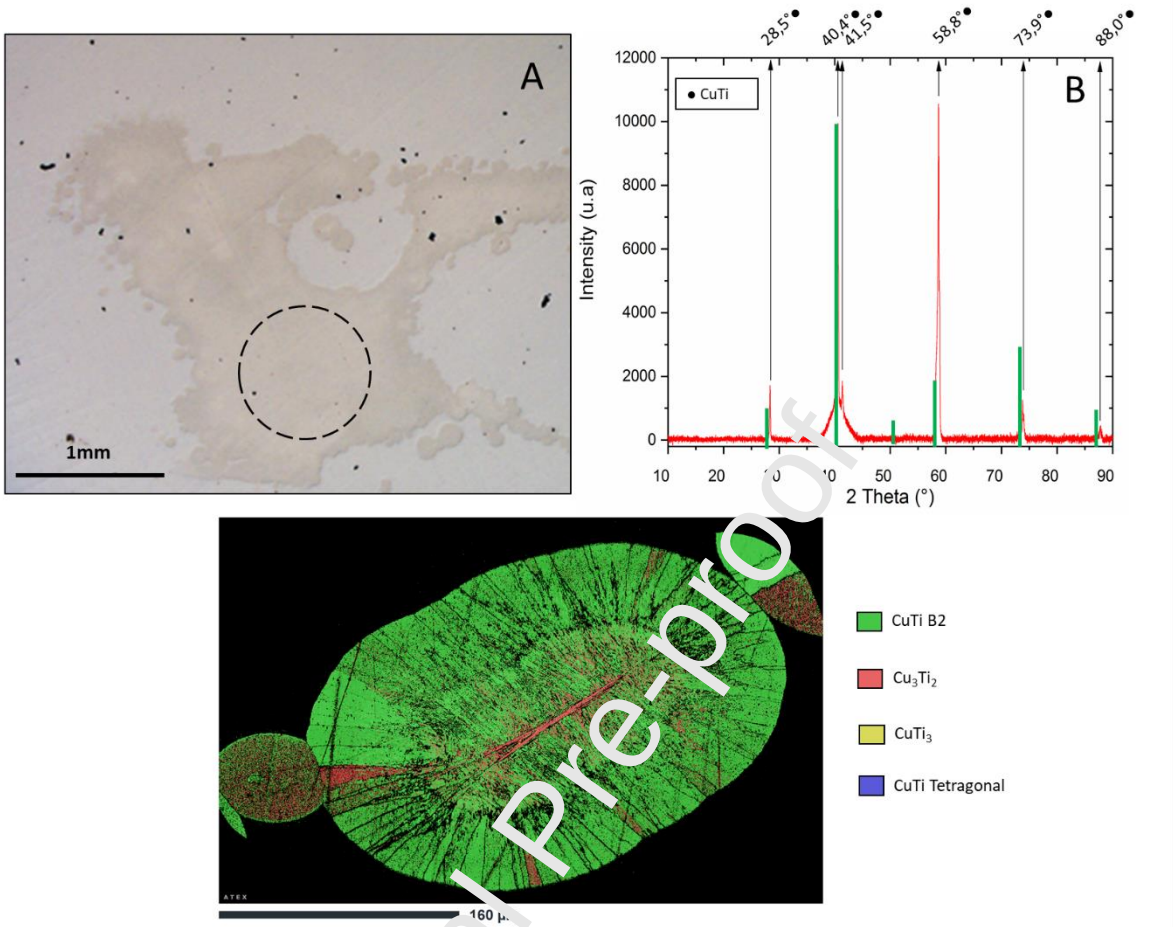

Figure 1: A) Illustration of spherulite aggregation region analysed using XRD. B) XRD pattern of large millimetric spherulite, confirming the presence of CuTi B2 phase as a major constituent. C) EBSD phase map of entire spherulite.

Many spherulites with diameters ranging from several tens to several hundreds of micrometres and randomly distributed were present in the rods. SEM–EDS analysis confirmed that the chemical composition of the amorphous phase (light-grey region in Figure 1A) corresponds to the nominal composition of the alloy, *i.e.*, $Ti_{40}Zr_{10}Cu_{36}Pd_{14}$. However, the spherulites (darker-grey region in Figure 1A) show a slight enrichment in Pd and a slight depletion in Cu, with a measured global composition of $Ti_{41}Zr_9Cu_{32}Pd_{18}$ and, thus, a very small change in chemical composition.

Figure 1B presents the diffractogram acquired in the area indicated in Figure 1A, which is an agglomeration of spherulites over a total area of several mm^2. The diffractogram contains six main peaks of high intensity. Phase identification was performed using the Rietveld method. The CuTi (cubic) phase with a lattice parameter of 3.14 Å matches well with the diffractogram, and the density of the [0 0 2] plane is somewhat larger than expected, indicating a possible preferred crystallographic orientation. No other phase could be identified from this diffractogram. EBSD analysis confirmed the XRD results, as most of the surface of the spherulites was indexed as the cubic CuTi B2 phase (Figure 1C). Note that the needle in the central part was indexed as the Cu_3Ti_2 phase. CuTi tetragonal and $CuTi_3$ were not detected at that scale on the spherulite.

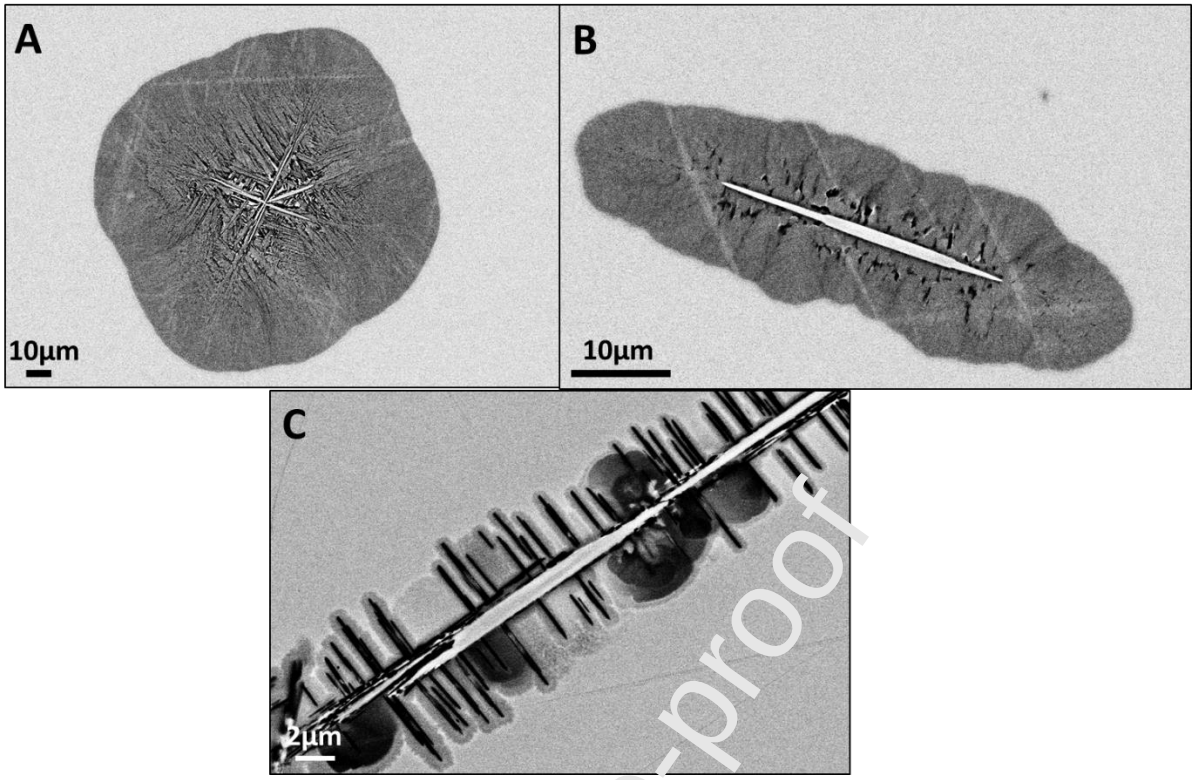

Figure 2: Examples of spherulites observed in the TiCuZrPd alloy in SEM –BSE mode: A) large spherulite of more than 100 µm in the core of the as-cast rod, B) smaller spherulite of a few micrometres in the periphery of the rod, and C) small needle-shaped defect, which corresponds to an earlier stage of crystal growth. In all cases, the core of the defect consisted of white long needles, together with a darker phase, from which a grey phase appears to be growing.

Three typical spherulite morphologies observed in the rods in SEM–BSE mode are presented in Figure 2. In Figure 2A, the spherical large spherulites, of approximately 140-µm diameter, consist of a much finer microstructure in the core than in the periphery. These spherulites are composed of long needles (length of approximately 50 µm and thicknesses of a few micrometres) that split in all directions, which appear bright. These needles will be referred to as 'primary needles'. Finer dark needles of a few micrometres long and a few tens of nanometres thick neighbour the bright needle and will be referred to as 'secondary needles'. Finally, these two phases are encircled by a grey phase, which grows with a spherical shape.

Similar contrasts and phase distributions were observed in the two other spherulite types, Figure 2B and Figure 2C, with smaller sizes and fewer needles. One bright long needle was also present, together with thinner dark needles (oriented perpendicularly to the bright needles), both surrounded by a grey phase. The arrangement and morphology of the phases are therefore very similar to that observed at the centre of the spherical spherulites in Figure 2A. Higher-magnification observations were performed to better understand the microstructure of these defects.

1. Phase identification at the core of the spherulites at the micrometre scale

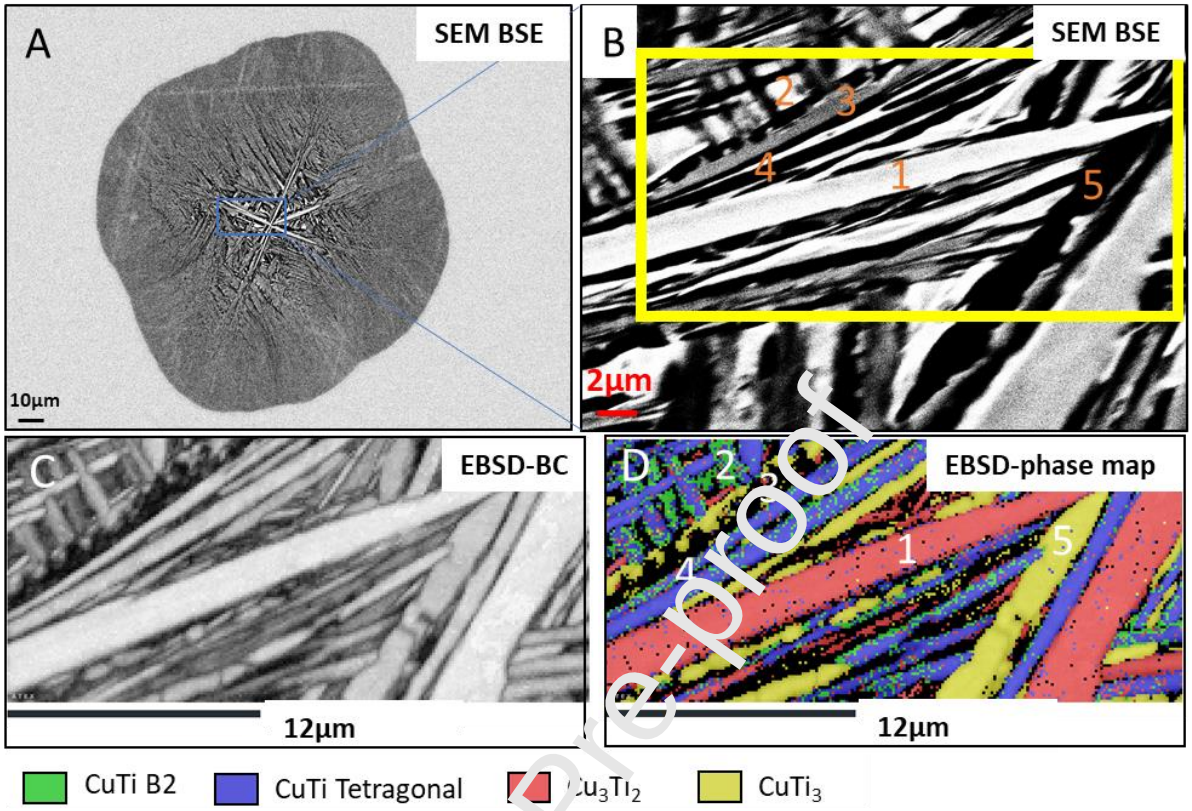

Figure 3: A) and B) SEM–BSE micrographs of core of a large spherulite at different magnifications. B shows the areas targeted for the EDS measurements (orange numbers). C) and D) band contrast map and EBSD map of phase repartition of image B).

Figure 3A and B present SEM–BSE micrographs of one large spherulite at two magnifications. In Figure 3B, at higher magnification, three contrasts are observed, indicating the presence of at least three different phases: white needles of width of approximately 2 µm (point 1), black needles of size of approximately 1 µm (point 4 and 5), and a more diffuse thinner grey phase (points 2 and 3). EDS measurements were performed at 20 keV, which corresponds to an interaction volume diameter of approximately 1.2 µm. Considering the size of the microstructure, the measured chemical composition might sometimes overlap with that of the neighbouring phase. Additionally, EBSD maps were acquired over the same area; the band contrast (BC) and phase maps are presented in Figure 3C and Figure 3D, respectively. The EDS and EBSD results are summarised in Table 2.

Five phases with distinct chemical compositions were identified:

1. The large white primary needles, with composition $Ti_{30}Cu_{44}Zr_6Pd_{20}$, are particularly rich in Cu and Pd. This phase was indexed as the Cu_3Ti_2 tetragonal phase. Its (Cu+Pd)/(Ti+Zr) ratio is 1.8, which is close to that expected for the Cu_3Ti_2 phase.
2. The homogeneous grey phase, with composition $Ti_{45}Cu_{33}Zr_{10}Pd_{12}$, exhibits a chemical composition close to the nominal one. It was indexed from EBSD as a cubic CuTi B2 phase, and its (Cu+Pd)/(Ti+Zr) ratio is close to 1.
3. The white phase close to the primary needle, with composition $Ti_{24}Cu_{40}Zr_{18}Pd_{18}$, is particularly rich in Zr and poor in Ti. It could not be indexed by EBSD, as no diffraction signal was collected from this area, most likely due to the small size of this phase structure.

4. The secondary black needles (oriented at 90° to the primary needle), with a measured composition of $Ti_{43}Cu_{28}Zr_{11}Pd_{18}$, exhibit a chemical composition very close to that of the homogeneous grey phase (2) with a slight increase in Pd. This phase was indexed as tetragonal CuTi, and its (Cu+Pd)/(Ti+Zr) ratio is close to 1.
5. The darker globular phase, with chemical composition $Ti_{60}Cu_{19}Zr_8Pd_{13}$, was surprisingly rich in Ti at the expense of copper. It was indexed as $CuTi_3$, although its (Cu+Pd)/(Ti+Zr) ratio is close to 0.5.

Table 2 : Summary of SEM–EDS point analysis of central parts of spherulites.

Point	Composition (at%)	Ratio (Cu+Pd)/(Ti+Zr)	Candidate phase (EDS)	Indexed phase (EBSD)
1	Ti_{30} Cu_{44} Zr_6 Pd_{20}	1.8	Cu_3Ti_2 or Cu_2Ti	Cu_3 Ti_2
2	Ti_{45} Cu_{33} Zr_{10} Pd_{12}	0.8	CuTi	CuTi B2
3	Ti_{24} Cu_{40} Zr_{18} Pd_{18}	1.4	Cu_2Ti	Non indexed
4	Ti_{43} Cu_{28} Zr_{11} Pd_{18}	0.8	CuTi	CuTi tetragonal
5	Ti_{60} Cu_{19} Zr_8 Pd_{13}	0.5	$CuTi_2$	$CuTi_3$

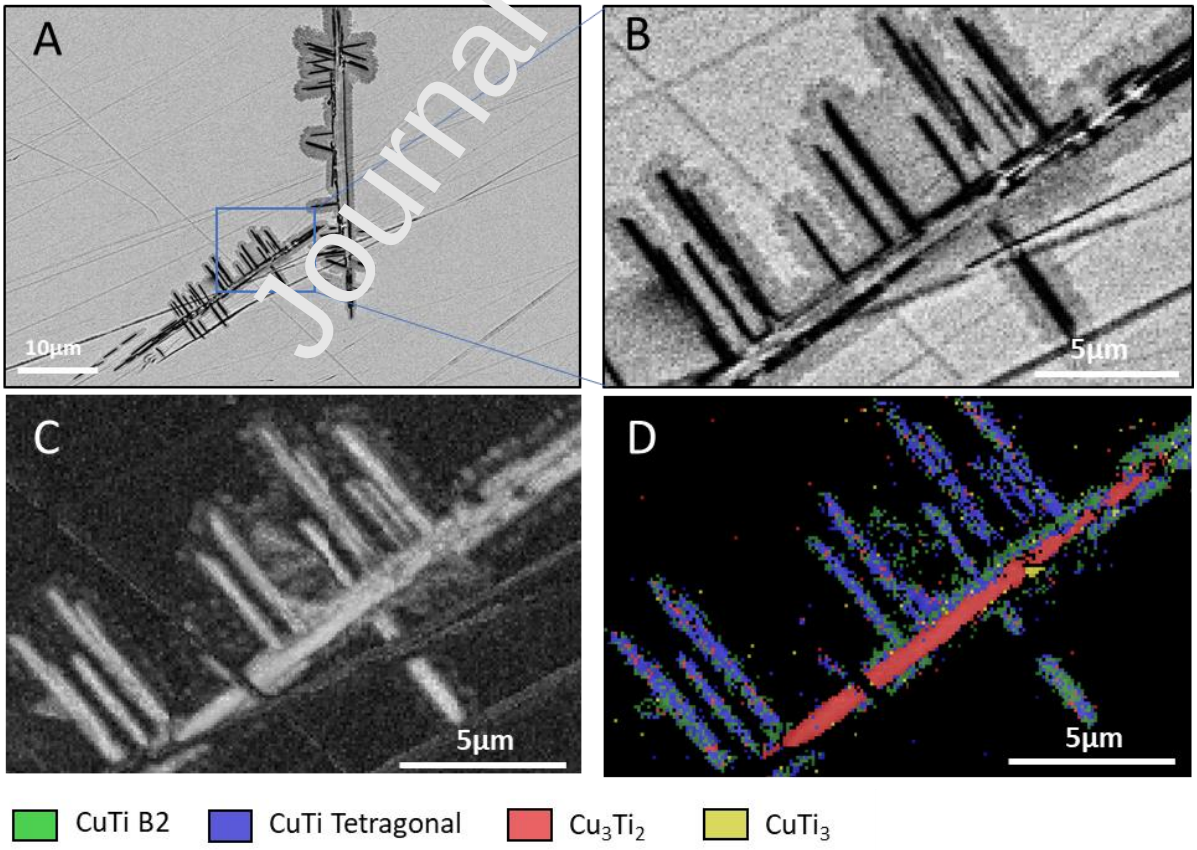

Figure 4: A) SEM–BSE micrograph of a needle-shaped defect at the periphery of the as-cast rod at different magnifications. B) Higher-magnification image of region in A. C) Corresponding band-contrast map. D) Corresponding EBSD map of phase repartition of image B.

Similar observations were performed on the other spherulite morphologies, see Figure 4. In this case, the microstructure was much simpler; only four phases were present in the spherulite's core. The 'primary needle' is indexed as the Cu_3Ti_2 phase, and the secondary needles as the CuTi tetragonal phase. At the periphery of the CuTi secondary needles, some areas may exhibit some chemical ordering, as they were indexed as the CuTi-B2 phase with the same orientation as the originating CuTi secondary needle. Note that when using EBSD, it is difficult to assess whether the phase is ordered or not, with the indexation observed for the core and the needles periphery being sometimes CuTi, sometimes CuTi-B2. Indeed, the diffraction patterns for both phases are very similar, and a dedicated indexation algorithm should be used to discriminate between the phases. Finally, the fourth phase, indexed as $CuTi_3$, was located close to the primary needle with a globular shape and a diameter of a few hundreds of nanometres.

2. Orientation relationship between the different phases

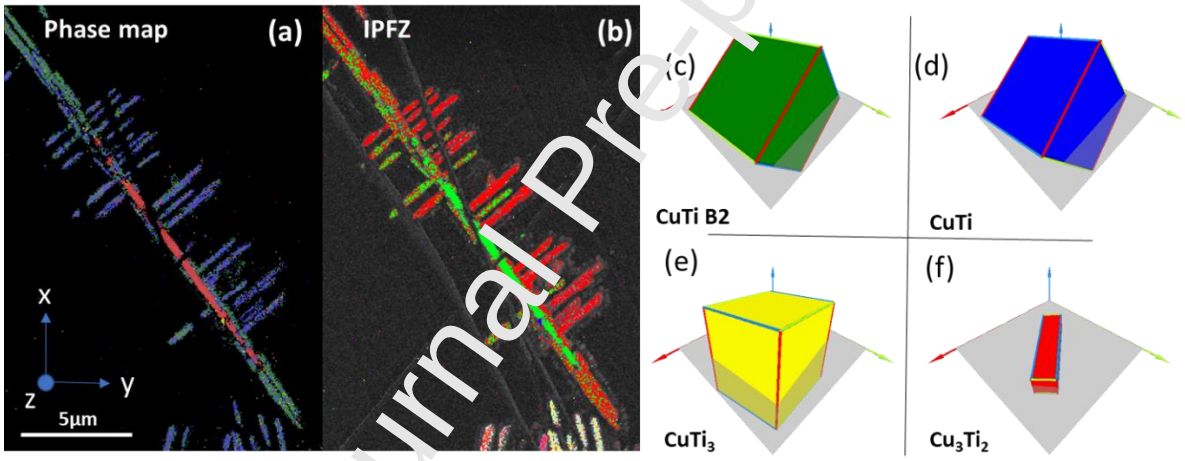

Figure 5: Orientation relationship between the four major phases, illustrated for the needle-shaped spherulites: (a) Phase map, (b) IPFZ orientation map, and orientation of (c) CuTi-B2, (d) CuTi tetragonal, (e) $CuTi_3$, and (f) Cu_3Ti_2 phases.

The same orientation relationship was observed between the major phases for all the spherulite morphologies (Figure 5):

$$<001>Cu_3Ti_2 \,//\, <001>CuTi \,//\, <001>CuTi_3$$
$$<010>\, Cu_3Ti_2 \,//\, <010>CuTi \,//\, <\text{-}110>CuTi_3$$

This finding confirms that the smaller spherulites did grow via the same mechanism as the large globular ones in Figure 2A and that the four phases identified are the main ones involved in their nucleation–growth mechanism.

To better describe and understand the microstructure of the large globular spherulites, additional TEM measurements were performed on a FIB foil extracted from the core of the spherulite.

3. Fine microstructure of the larger spherulites at the nanometric scale

A detailed characterisation of the microstructure of the largest spherulites at the nanometric scale revealed that their microstructure is even more complex and finer than that described from SEM.

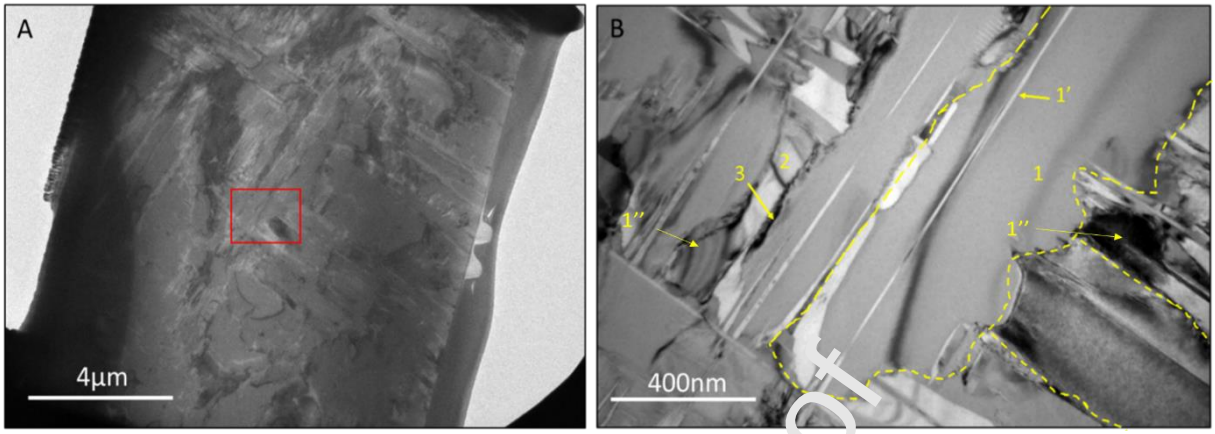

Figure 6: Low-magnification TEM images of FIB foil extracted from the centre of a large spherulite. Image B is a zoom-in of the area indicated in red in image A.

Indeed, Figure 6A presents a general view of the thin foil extracted at the centre of the spherulite, revealing a much finer microstructure than that described from SEM observation. In Figure 6B, several wide needles, corresponding to the primary or secondary ones observed from SEM, are visible and encircled by a yellow dashed line (noted as 1 in Figure 6B). One can notice that the needles are all perpendicular to each other, such as for the 'small' spherulites observed previously by SEM. Bright thin laths of a few nanometre thickness are present in the middle of those primary laths (1'). The CTEM contrast on those large laths indicate that some of them are distorted (1"), and internal stress might have appeared during the simultaneous growth of the different needles. The primary laths interface is tortuous and decorated with secondary phases. For instance, a dark phase of a few nanometres thick is visible (3) as well as white phases in between the laths (2).

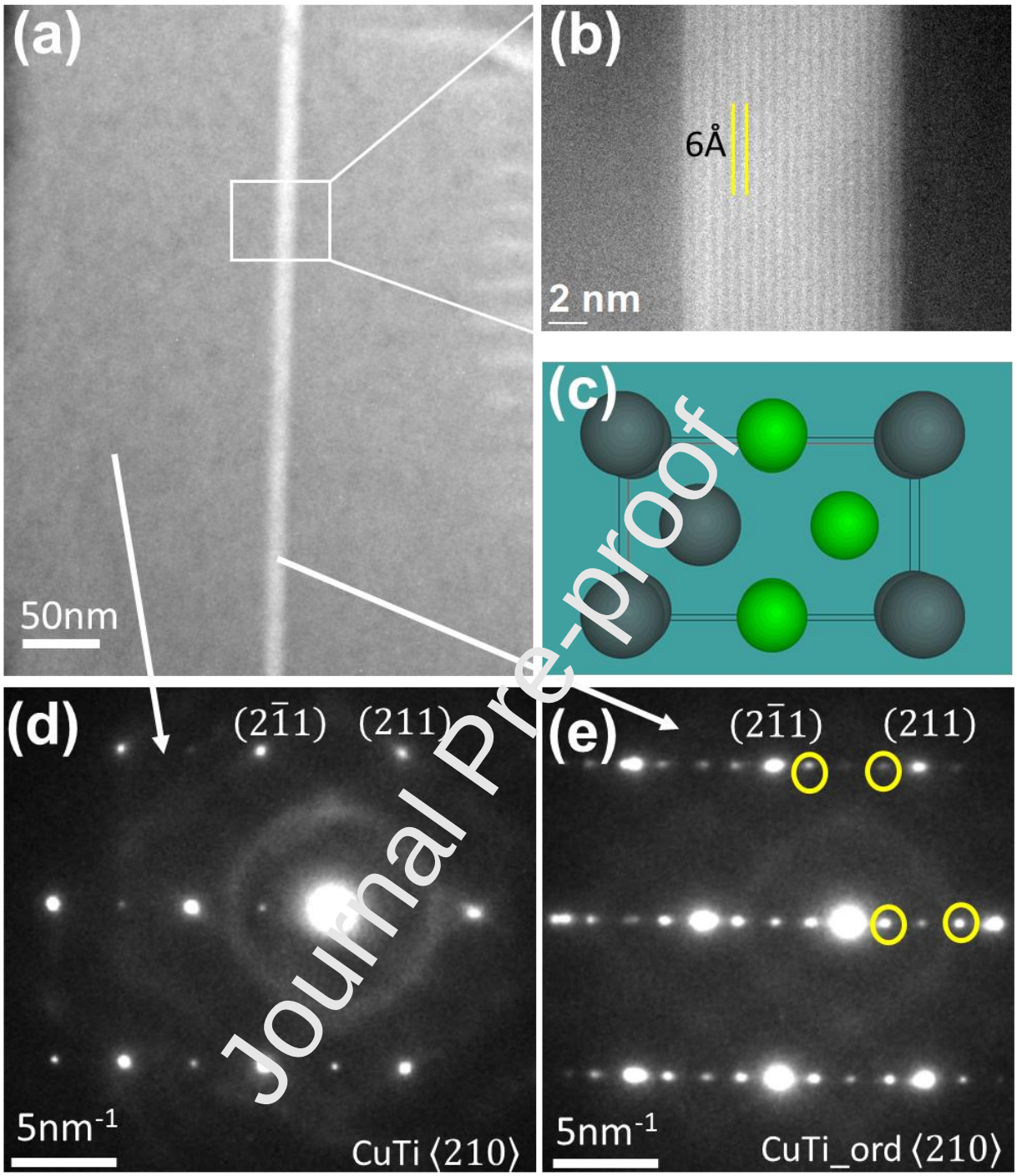

Figure 7: (a) CTEM micrograph of CuTi laths and (b) corresponding SAED pattern, indicating a <210> orientation of the Cu-Ti tetragonal phase (d). (b) An additional phase, of few nanometres in thickness, for which a 6-Å periodicity is visible in that orientation, already described in [17].(e) corresponding SAED pattern, the ordering leads to the presence of additional spots, which were successfully indexed as the CuTi-ordered phase with zone axis <210>, the lattice is illustrated in (c).

The major grey phase (1 in Figure 6B) was identified using SAED, Figure 7(a) and (b), as the CuTi-tetragonal phase, which is in good agreement with previous XRD and SEM–EBSD characterisation. The 1’ phase, which appears as long white stripes in Figure 7(a) has a periodicity of 6 Å (Figure 7(c)). This phase presents the same electron pattern as the CuTi laths, with additional spots, typical for the chemical ordering in Figure 7(e). This additional ordering is that presented in [17], with an

intermediate long-period structure (a = 3.13 Å and c= 5.919 Å). Thus, the CuTi-tetragonal phase undergoes chemical ordering after formation.

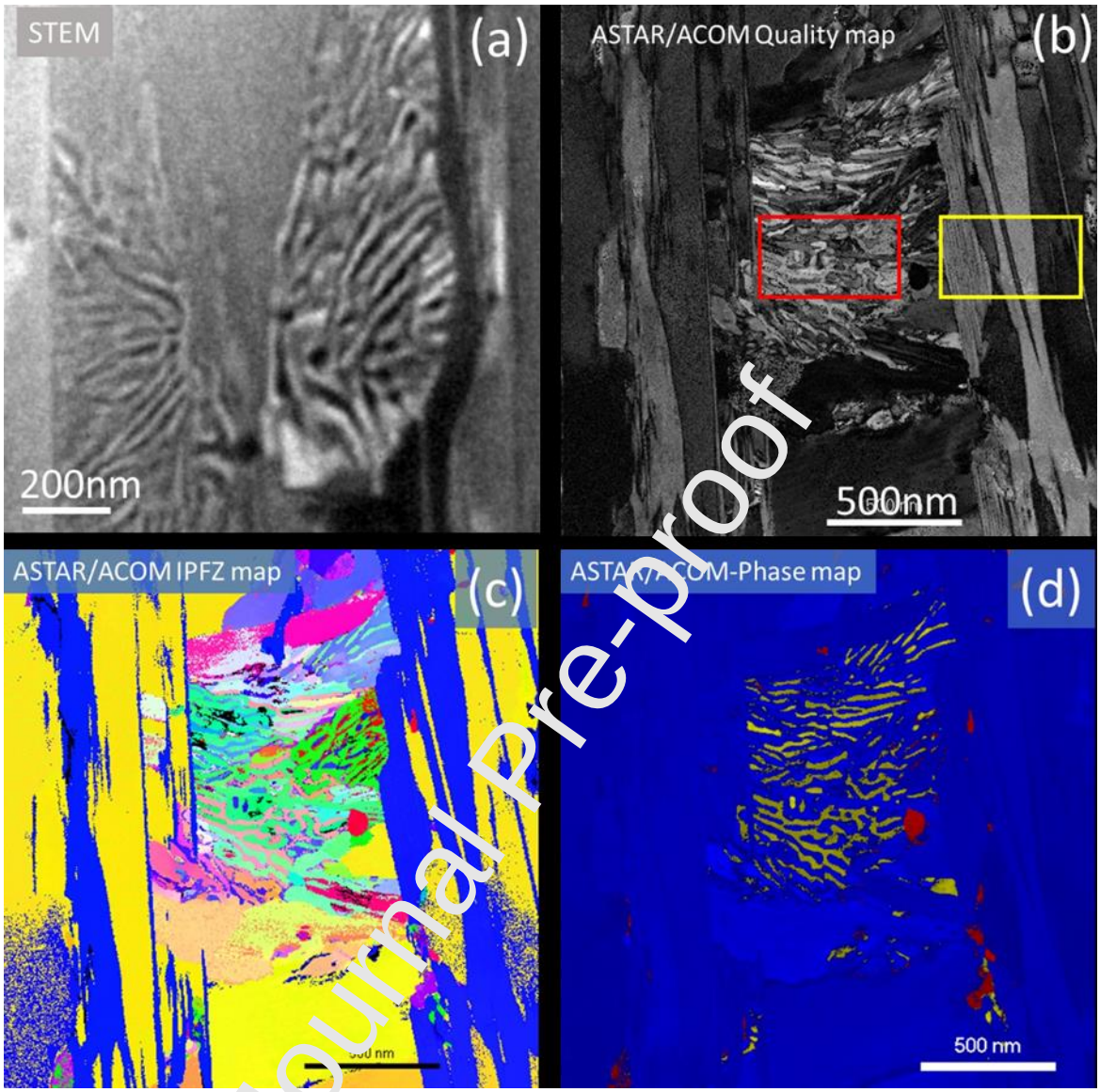

Figure 8: Evidence of phase decomposition occurring in the CuTi phase, observed using (a) STEM, with Z contrast, and (b–d) ASTAR/ACOM orientation mapping on another area. (b) Quality map of analysed area. (c) Corresponding orientation IPFZ map and (d) corresponding phase map with three identified phases (CuTi-tetra in blue, Cu_3Ti_2 in red, and $CuTi_3$ in yellow).

Additionally, a typical eutectoid-like structure was observed within the CuTi laths, with a-few-nanometre-thick lamellas, see Figure 8(a). Orientation mapping performed using TEM with the ACOM/ASTAR tool enabled the product of the eutectoid reaction to be identified as CuTi and $CuTi_3$ (see red squared area in Figure 8(b)). The orientation map indicates that the CuTi phase present in the eutectoid aggregate does not have the same orientation as the initial CuTi lath (Figure8(c)). The reaction appears to start at the interface and propagate within the lath. Additionally, a few nodules of the Cu_3Ti_2 phase were observed close to the decomposed area.

4. Microstructure of interface between large spherulites and amorphous matrix

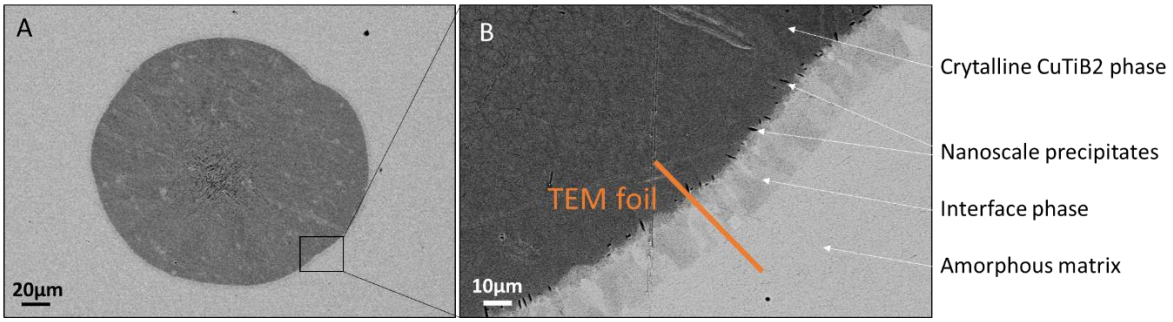

Figure 9: SEM–BSE images of spherulite/matrix interface: A) low-magnification image of spherulite and B) detailed view of black rectangular zone in A), revealing the presence of nanoscale-sized dark precipitates as well as an interface shell of approximately 3–4-µm thickness

SEM–BSE micrographs of the interface between the spherulite and amorphous matrix are presented in Figure 9. At the crystalline/amorphous interface, an intermediate phase of approximately 3 and 4 µm in thickness is visible with light-grey contrast. This contrast might arise from chemical contrast and/or crystallographic contrast. This shell is present around all spherulites and likely consists of columnar grains. Black nanometric precipitates with elongated shape and dark contrast are also present at the interface between the spherulite and shell. Most of these precipitates are oriented 45° relative to the interface. To better analyse the chemical composition and crystallographic nature of this region, a thin foil was extracted using FIB at a localisation similar to that indicated by the orange line in Figure 9B.

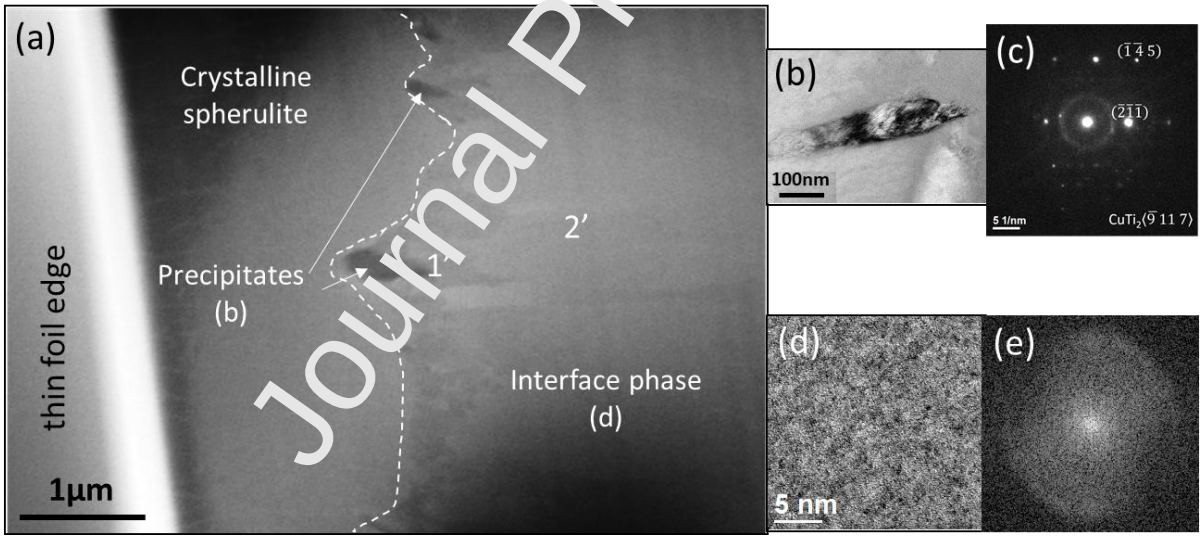

Figure 10: A) SEM observation of FIB lamella extracted at the interface of the spherulite. Two distinct areas are visible: the crystalline spherulite on the left, composed mainly of the CuTi phase, from previous observations, and the interfacial region on the right. B) and C) TEM CTEM micrograph of precipitate and corresponding FFT pattern. D) and E) higher-magnification TEM micrograph of interfacial area and corresponding FFT pattern. The noted numbers 1' and 2' are the positions where the EDS measurements were performed, and the results are reported in Table 3.

Figure 10 presents the localisation of the chemical analysis realised at the interface. The corresponding measurements are presented in Table 3.

Table 3: Chemical measurements performed using SEM on the thin foil extracted at the interface

Point	Composition (at%)	(Cu+Pd) /(Ti+Zr) ratio	Phase candidate	SAED diffraction

1'	$Ti_{47}Cu_{20}Zr_{12}Pd_{21}$	0.7	Cu_2Ti_3	$CuTi_3$
2'	$Ti_{37}Cu_{25}Zr_{14}Pd_{23}$	1	CuTi	Amorphous

The chemical composition of the precipitates corresponds to $Ti_{47}Cu_{20}Zr_{12}Pd_{21}$. The precipitates are rich in Ti and Pd. From TEM SAED, one precipitate was indexed as the $CuTi_3$ phase.

The chemical composition of the shell is $Ti_{37}Cu_{25}Zr_{14}Pd_{23}$, indicating a local enrichment in Zr and Pd compared with the nominal composition of the alloy. The Cu+Zr/Ti+Pd ratio is close to 1. A higher-magnification micrograph of the interfacial region is presented in Figure 10d. Surprisingly, this area that shows a contrast typical for columnar grains presents no atom arrangement. Its corresponding FFT pattern is diffuse, indicating that the area is amorphous.

3. Discussion

Numerous spherical crystalline aggregates, of several hundred micrometres and randomly dispersed, were observed in suction casting parts of the $Ti_{40}Cu_{36}Zr_{10}Pd_{14}$ alloy. The presence of such spherulites is not often reported in the literature. Multi-scale electron microscopy observations revealed that their microstructure is complex.

Thanks to the composition measurements of the indexed phases and the EBSD measurements, reliable quantification of the different phases was performed. Only phases containing the two major elements of the grade, i.e., Cu and Ti, were considered as possible solutions. This rather simple assumption is first based on previous literature results [15,16] and second coherent with the fact that Zr and Pd have electronic structures and atomic radii that allow them to substitute for Ti and Cu, respectively [12]. All the results (XRD patterns, EBSD maps, and EDS, SAED–TEM, and ASTAR TEM analyses) were consistent with this hypothesis, and it was observed that the major phases present have similar structures as Cu_3Ti_2, CuTi (tetragonal and B2 cubic), and $CuTi_3$.

All the spherulite morphologies presented the same phase arrangement: a primary needle with a similar structure as the Cu_3Ti_2 phase surrounded by perpendicular secondary needles of the CuTi-tetragonal phase. A third phase, with a macroscopic globular shape, indexed as the $CuTi_3$ phase is also present between the needles. All these phases are surrounded by large globular grains of the CuTi B2 phase. Note that for all the morphologies and spherulite sizes, the dimensions of the primary and secondary needles (between 20- and 40-µm long and 1- and 2-µm wide) as well as their orientation relationships (see Figure 2) remained unchanged. Therefore, these phases are considered as the precursor.

Some areas were nevertheless not indexed using EBSD mapping, which is due to their nanometric size. At an even finer scale, using TEM ASTAR ACOM orientation mapping, structures typical for a eutectoid reaction were observed (Figure 8). The product phases were identified as CuTi and $CuTi_3$. For a CuTiZrNi amorphous alloy, Yang *et al.*[15] reported that the CuTi phase is unstable and undergoes a eutectoid reaction that also forms $CuTi_3$ among other phases. A similar type of reaction is expected for the present alloy, and the presence of this eutectoid aggregate indicates that the initial CuTi-tetragonal phase is not stable.

Additionally, a chemical ordering was observed in some of the CuTi-tetragonal needles, resulting in the appearance of nanometric large domains presenting long-range chemical ordering (Fig. 7). This phenomenon was already reported by Marschall [17] in an amorphous CuTi binary alloy. As this type

of structure was only observed in the core of the large spherulites and not in the early structures, this decomposition occurs after the formation of the spherulite (in the solid state).

A growth scenario was deduced from these observations and is illustrated in Figure 11.

As described in Figure 11, after nucleation, the Cu_3Ti_2 primary needle acts as a nucleation site for the other phases. These primary needles are enriched in Cu and Pd and poorer in Ti compared with the amorphous matrix. Thus, there is a diffusion flux of Ti from the needle towards the interface while the Cu and Pd diffuse from the matrix towards the primary needle. Therefore, a depletion of Cu around the needle is observed, which leads to the appearance of the secondary CuTi tetragonal needles (Figure 11A), which are poorer in Cu compared with the matrix (composition $Ti_{45}Cu_{28}Zr_{11}Pd_{18}$). These needles do grow perpendicularly to the primary ones, and the orientation relationship between the two phases is the following: <001> Cu_3Ti_2//<001>CuTi and (001)Cu_3Ti_2//(001)CuTi. Finally, a third phase appears, with a composition really close to that of the amorphous matrix and a globular shape and with a similar phase structure as CuTi-B2 (Figure 11B). This phase might crystallise from the interface of the primary and secondary needles towards the amorphous matrix. For spherulites located in the core of the rods, CuTi globular grains encapsulate several needles in a spherical shape (Figure 2A and Figure 11D), whereas for the ones located closer to the external surface, the globular grains were smaller than the secondary needles (see 2B and Figure 11C). This finding indicates that the cooling rate may affect the growth kinetics of the spherulites. At a slower cooling rate, the CuTi B2 globular grains have more time to grow and encapsulate the needles. Finally, as CuTi-tetragonal is not stable, a eutectoid reaction can occur, leading to the appearance of CuTi and $CuTi_3$ laths, see Figure 11F. Some CuTi laths also undergo an additional chemical ordering, with the appearance of nanometre-thick ordered laths (Figure 11E). Finally, the interface between the crystallised material and amorphous matrix is described in Figure 11G. This particular organisation may enable the material to have a more thermodynamically stable interface.

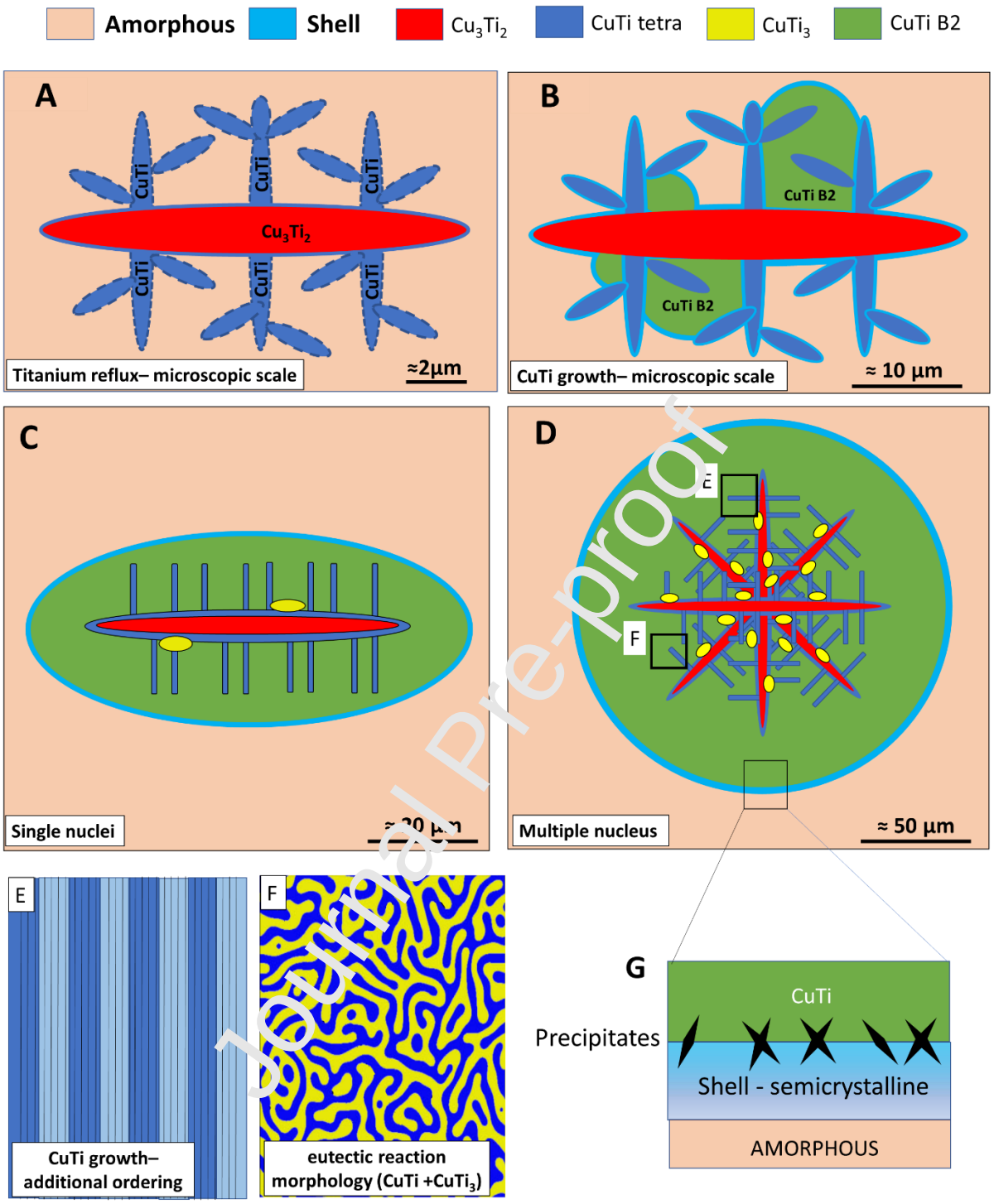

Figure 11: Schematic representation of the growth mechanism proposed for the spherulites. A, Rejection of Ti away from the Cu3Ti2 primary needles (red) and subsequent formation of CuTi secondary needles (dark blue) B, Apparition of ordered CuTi B2 (green) around the secondary needles. C, Resulting microstructure observed for small spherulites composed of a single nuclei of Cu_3Ti_2. D) Microstructure of larger spherulites, revealing the presence of several Cu_3Ti_2 primary needles. Additional phases are observed within these large spherulites with nano-scale ordering of the CuTi phase (E) and the formation of the $CuTi_3$ phase through a eutectic reaction (F). G, The shell of the large spherulites is composed of nano-scale precipitates and a semi-crystalline layer.

The exact reasons for the nucleation of the Cu_3Ti_2 primary needle remain unknown. The mechanism proposed here described the development of the spherulites after the apparition of the Cu_3Ti_2 primary needles, as no other phase is observed from those post mortem observations. It cannot be excluded that the amorphous phase could undergo a phase transformation to a metastable phase that is not

present any more after solidification. This metastable phase could be linked with the presence of the semicrystalline shell, such as observed in [JAL 2020].

This could occur before solidification, in the liquid phase or within the solid amorphous phase. No evolution was observed in the microscopy analyses during heat treatment at 500°C (just below T_g) of the sample, indicating that the amorphous phase is rather stable. Moreover, larger spherulites were mainly observed in larger rods or in the core of the rod, indicating that the cooling rate has a direct effect on the growth rate of the spherulites. Therefore, we assume that the germs are most likely present in the liquid phase during casting. Small longitudinal spherulite precursors, as illustrated in Figure 11C, contain only one primary needle of Cu_3Ti_2, whereas the large spherulites (Figure 11D) contain many Cu_3Ti_2 needles. This indicates that the nucleation of the primary needle, with one or more needles, directly affects the final shape and size of the spherulites.

Although the dominating mechanism leading to the nucleation of the spherulites remains unknown, several hypotheses can be proposed. First, there may be not enough melting steps before the casting of the rod, which could result in non-melted areas or non-chemically homogeneous areas, therefore still organised areas at a very small scale. It is known that germination sites can be very small (a few nanometres) [22]. Second, it is also possible that the cooling rate applied is not high enough to avoid the crystallisation nose of the Cu_3Ti_2; the enthalpy of crystallization may be too low to be avoided [23]. Third, it is possible that the Cu_3Ti_2 nucleation is encouraged by Pd and Cu gathering, indeed, the mixing enthalpy is very negative for Pd and Ti and Zr (-65 and -91kJ/mol respectively) whereas it is less important for Pd and Cu (-14 kJ/mol) [24]. This could give rise to a clustering of Cu and Pd in the amorphous phase, and later on the formation of the Cu_3Ti_2 primary needle (the phase richest in Cu and Pd see Table 2). Another hypothesis can be the presence some impurities/pollution in the pure metalss or oxygen/hydrogen contamination during the casting that act as preferential nucleation sites for Cu_3Ti_2.

Several studies suggest that spherulites may affect the mechanical properties. According to [25,26], if the spherulites have a diameter below 100 µm, plasticity before failure can be observed. This has been verified in this system in [8]. The presence of small, ductile spherulites in the amorphous matrix may generate a composite-material behaviour but may induce a brittle behaviour for larger sizes. Composite metallic glasses are mainly known for ZrCu and TiNi grades [27], the aim being to control the volume fraction of the crystalline phase to maintain a high mechanical strength while having a plastic deformation before failure in compression. The amorphous fraction is free of grains and of grain boundaries with no residual dislocations/stresses, giving it a very high R_m and a very high elastic energy storage. The crystalline fraction identified as the B2 ZrCu phase has, via a martensitic-type transformation (under stress), the ability to transform into the B19' phase, which macroscopically provides a lot of ductility. There is a blocking effect already documented in the literature that slows down crack propagation (increase in cell volume from B2 to B19')[28]. Although several studies have suggested that the same phenomena occur for TiCu grades [27], these are much less studied, and there is no published data in this sense for the grade studied here. As illustrated in Figure 8, decomposition and ordering structures are indicators of a potential phase transformation.

To better control the mechanical properties of the material, the size of the spherulites must be controlled, which can be realised using different methods. The first one consists of targeting the best glass-forming ability (GFA) alloy composition, as illustrated in the work of Sypien et al. [29] who studied this type of alloy with 10, 14, and 20 at% Pd (replacing Cu). A simple calculation of GFA = $T_{x1}/(T_g+T_l)$ suggests that the alloy with 14 at% Pd has the smallest GFA. It is probable that a small change in composition could decrease the enthalpy of crystallisation and then reduce the volume fraction of crystals in the rods; however, to our knowledge, this analysis has never been performed.

The second and most important parameter for the size-distribution control is the casting process. Arc-melter suction casting does not allow precise control of the temperature, raising some questions about the master-alloy chemical homogeneity (and the number of melting steps required [22]) and the intensity of the arc used should be investigated in future studies.

The control of casting parameters is an important issue for the future industrialisation of metallic glass, particularly in the medical sector (among others). Spherulites are defects found in many ZrCuNi BMGs, with different microstructure/size and distribution characteristics. The understanding of the growth scenario those spherulites can help the BMG community to improve the casting conditions and address the casting defect issue and have more predictable mechanical properties. The above-mentioned leads are elements to be explored in order to consider an industrialization of this BMG composition for the manufacture of dental implants.

4. Conclusion

This paper focused on a detailed description of the fine microstructure of crystalline spherulites embedded in an amorphous matrix of the $Ti_{40}Cu_{36}Zr_{10}Pd_{14}$ BMG alloy. This study reveals a complex microstructure very fine in the core (with two types of needles) and less and less complex until reaching the interface with the amorphous matrix. This interface contains precipitates of $CuTi_3$ and a not fully organised shell. Thanks to EDS chemical composition analyses and the use of the CuTi binary diagram, candidate phases were proposed and tested in EBSD and on diffraction images from TEM analysis. The following phase structures were formally identified: Cu_3Ti_2, $CuTi_3$, CuTi B2, and CuTi tetragonal. These phases are always observed at the same place in the spherulites and with the same orientation relationship to each other.

Spherulite structures at different stages of growth (from primary to mature) were observed, allowing us to propose a growth process consisting of the following main steps:

1. Formation of large needles of the Cu_3Ti_2 phase (primary needles)

2. This phase is surrounded by a second phase with finer needles oriented at 90° of a phase close to CuTi tetragonal (secondary needles). During solidification, a eutectoid reaction occurs, which leads to the appearance of a small amount of $CuTi_3$.

3. The entire structure is surrounded by a semi-crystalline shell, which ensures the transition between order and disorder.

4. The CuTi B2 phase is present in majority in mature spherulites (the other phases are only present in the centre part). It grows between the CuTi tetragonal phase and the shell in all directions until the temperature is too low to allow atomic movements, giving the spherical shape to the spherulites.

Acknowledgments

The authors would like to thank Xavier Boulnat for his help with and training in the arc-melting suction casting process and Laurent Gremillard for his help with the Rietveld method applied to the XRD pattern of the alloy. The authors would also like to thank the Agence National de la Recherche (ANR) and its funding within the framework of the ANR-TNT-. The authors acknowledge the 'Réseau Renatech' and the assistance of David Troadec in the preparation of the FIB thin foils at IEMN (https://www.renatech.org/). Finally, the authors acknowledge Nicholas Blanchard for access to the TEM JEOL 2010 of the Centre Lyonnais de Microscopy (www.clym.fr).

References

[1] M. Chen, A brief overview of bulk metallic glasses, NPG Asia Mater. 3 (2011) 82–90. https://doi.org/10.1038/asiamat.2011.30.

[2] J.R. Scully, A. Gebert, J.H. Payer, Corrosion and related mechanical properties of bulk metallic glasses, J. Mater. Res. 22 (2007) 302–313. https://doi.org/10.1557/jmr.2007.0051.

[3] G. Duan, A. Wiest, M.L. Lind, J. Li, W.K. Rhim, W.L. Johnson, Bulk metallic glass with benchmark thermoplastic processability, Advanced Materials. 19 (2007) 4272–4275. https://doi.org/10.1002/adma.200700969.

[4] A. Liens, A. Etiemble, P. Rivory, S. Balvay, J.M. Pelletier, S. Cardinal, D. Fabrègue, H. Kato, P. Steyer, T. Munhoz, J. Adrien, N. Courtois, D.J. Hartmann, J. Chevalier, On the potential of Bulk Metallic Glasses for dental implantology: Case study on Ti 40 Zr 10 Cu 36 Pd 14, Materials. 11 (2018). https://doi.org/10.3390/ma11020249.

[5] S.L. Zhu, X.M. Wang, F.X. Qin, A. Inoue, A new Ti-based bulk glassy alloy with potential for biomedical application, Materials Science and Engineering: A. 459 (2007) 233–237. https://doi.org/10.1016/j.msea.2007.01.044.

[6] M. Calin, A. Gebert, A.C. Ghinea, P.F. Gostin, S. Abdi, C. Mickel, J. Eckert, Designing biocompatible Ti-based metallic glasses for implant applications, Materials Science and Engineering C. 33 (2013) 875–883. https://doi.org/10.1016/j.msec.2012.11.015.

[7] D.C. Hofmann, Bulk Metallic Glasses and Their Composites: A Brief History of Diverging Fields, Journal of Materials. 2013 (2013) 1–8. https://doi.org/10.1155/2013/517904.

[8] L. Gautier, A. Liens, B. Ter-Ovanessian, S. Marcelin, F. Douillard, H. Richard, N. Courtois, J. Chevalier, D. Fabrègue, Impact of spherulite-type crystalline defects on the mechanical and electrochemical properties of TiCuZrPd metallic glasses, Materialia. (2022) 101353. https://doi.org/10.1016/j.mtla.2022.101353.

[9] A. Sypien, T. Czeppe, G. Garzel, L. Litynska-Dobrzynska, J. Latuch, N.Q. Chinh, Thermal stability and mechanical properties of the TiCuZrPd glasses with 10, 14 and 20at.% Pd, Journal of Alloys and Compounds. 615 (2014) S108–S112. https://doi.org/10.1016/j.jallcom.2013.12.240.

[10] T. Czeppe, A. Sypien, A. Wierzbicka-Miernik, Modification of the Ti40Cu36Zr10Pd14 BMG Crystallization Mechanism with Heating Rates 10-140 K/min, J. of Materi Eng and Perform. 25 (2016) 5289–5301. https://doi.org/10.1007/s11665-016-2368-x.

[11] H. Okamoto, Pd-Ti (Palladium-Titanium), J. Phase Equilib. Diffus. 34 (2013) 74–75. https://doi.org/10.1007/s11669-012-0137-6.

[12] K.C. Hari Kumar, P. Wollants, L. Delacy, Thermodynamic assessment of the Ti-Zr system and calculation of the Nb-Ti-Zr phase diagram, Journal of Alloys and Compounds. 206 (1994) 121–127. https://doi.org/10.1016/0925-8388(94)90019-1.

[13] S.H. Hong, Mechanical, deformation and fracture behaviors of bulk metallic glass composites reinforced by spherical B2 particles, Progress in Natural Science. (2018) 7. https://doi.org/10.1016/j.pnsc.2018.11.001.

[14] B. Beausir, J.-J. Fundenberger, Analysis Tools for Electron and X-ray diffraction, ATEX - software, Université de Lorraine - Metz, 2017. www.atex-software.eu.

[15] Y.J. Yang, R. Zhou, S.D. Wei, D.Y. Liu, H.L. Xu, S.L. Li, Microstructural evolution of slowly solidified Cu-Ti-Zr-Ni amorphous alloy, Journal of Non-Crystalline Solids. 357 (2011) 1516–1521. https://doi.org/10.1016/j.jnoncrysol.2010.12.043.

[16] J. Fornell, N. Van Steenberge, A. Varea, E. Rossinyol, E. Pellicer, S. Suriñach, M.D. Baró, J. Sort, Enhanced mechanical properties and in vitro corrosion behavior of amorphous and devitrified Ti40Zr10Cu38Pd12 metallic glass, Journal of the Mechanical Behavior of Biomedical Materials. 4 (2011) 1709–1717. https://doi.org/10.1016/j.jmbbm.2011.05.028.

[17] A.F. Marshall, Y.S. Lee, D.A. Stevenson, Crystallization behavior of amorphous Cu48Ti52: Formation of an intermediate long-period superlattice phase, Acta Metallurgica. 35 (1987) 61–68. https://doi.org/10.1016/0001-6160(87)90213-6.

[18] V.N. Eremenko, Yu.I. Buyanov, S.B. Prima, Phase diagram of the system titanium-copper, Powder Metall Met Ceram. 5 (1966) 494–502. https://doi.org/10.1007/BF00775543.
[19] N. Karlsson, An x-ray study of the phases in the copper-titanium system, J Inst Met. 79 (1951) 391–405.
[20] A.V. Zhalko-Titarenko, M.L. Yevlashina, V.N. Antonov, B.Yu. Yavorskii, Yu.N. Koval, G.S. Firstov, Electronic and Crystal Structure of the ZrCu Intermetallic Compound Close to the Point of Structural Transformation, Physica Status Solidi (b). 184 (1994) 121–127. https://doi.org/10.1002/pssb.2221840108.
[21] E.F. Rauch, M. Véron, Automated crystal orientation and phase mapping in TEM, Materials Characterization. 98 (2014) 1–9. https://doi.org/10.1016/j.matchar.2014.08.010.
[22] Y. Hu, J. Li, T. Lin, Y. Zhou, Plasticity improvement of Zr55Al10Ni5Cu30 bulk metallic glass by remelting master alloy ingots, J. Mater. Res. 24 (2009) 3590–3595. https://doi.org/10.1557/jmr.2009.0430.
[23] A. Inoue, Stabilization of metallic supercooled liquid and bulk amorphous alloys, Acta Materialia. 48 (2000) 279–306. https://doi.org/10.1016/S1359-6454(99)00300-6.
[24] S.L. Zhu, X.M. Wang, F.X. Qin, M. Yoshimura, A. Inoue, New Ti–Zr–CuPd Quaternary Bulk Glassy Alloys with Potential of Biomedical Applications, Mater. Trans. 48 (2007) 2445–2448. https://doi.org/10.2320/matertrans.MRA2007086.
[25] S. Hin, C. Bernard, V. Doquet, Y. Yokoyama, A. Magueresse, V. Keryvin, Influence of as-cast spherulites on the fracture toughness of a Zr 55 Cu 30 Al 10 Ni 5 bulk metallic glass, Materials Science and Engineering: A. 740–741 (2019) 137–147. https://doi.org/10.1016/j.msea.2018.10.061.
[26] Z. Liu, R. Li, G. Liu, W. Su, H. Wang, Y. Li, M. Shi, X. Luo, G. Wu, T. Zhang, Microstructural tailoring and improvement of mechanical properties in CuZr-based bulk metallic glass composites, Acta Materialia. 60 (2012) 3128–3139. https://doi.org/10.1016/j.actamat.2012.02.017.
[27] Y. Chen, C. Tang, J.-Z. Jiang, Bulk metallic glass composites containing B2 phase, Progress in Materials Science. (2021) 100799. https://doi.org/10.1016/j.pmatsci.2021.100799.
[28] J. Zhou, H. Wu, Y. Wu, W. Song, R. Chen, C. Tan, G. Xie, D. Cao, H. Wang, X. Liu, S. Jiang, X. Wang, Z. Lu, Enhancing dynamic mechanical properties of bulk metallic glass composites via deformation-induced martensitic transformation, Scripta Materialia. 186 (2020) 346–351. https://doi.org/10.1016/j.scriptamat.2020.05.012.
[29] A. Sypien, K. Badura, P. Fima, K. Miernik, Effect of Pd, temperature and time on wetting and interfacial microstructure of bulk metallic glasses TiCuZrPd on Ti-6Al-4V substrate, Journal of Alloys and Compounds. 695 (2017) 962–970. https://doi.org/10.1016/j.jallcom.2016.10.216.

Conflict of Interest

The authors declare no conflict of interest.

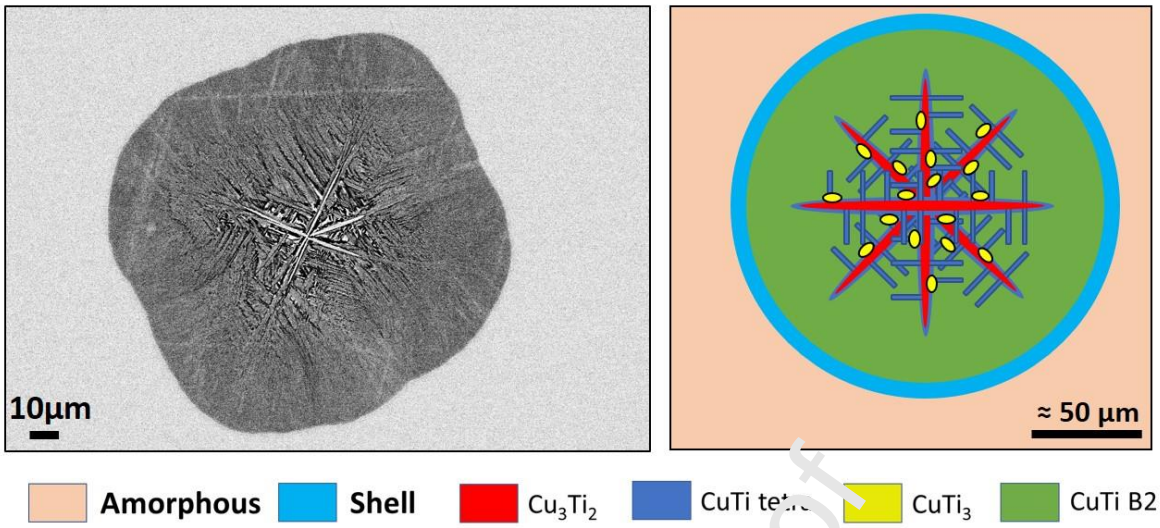

Highlights

- Multiscale characterization of spherulites in Ti-based BMG alloy
- Identification of the present phases: TiCu, TiCu B2, Ti_2Cu_3 and $CuTi_3$
- Growth scenario proposed for the spherulites